

Partha S. Pal · Harinder P. Singh · Kwing L. Chan ·
M. P. Srivastava

Turbulent Compressible Convection with Rotation - Penetration above a Convection Zone

Received: date / Accepted: date

Abstract We perform Large eddy simulations of turbulent compressible convection in stellar-type convection zones by solving the Navier-Stokes equations in three dimensions. We estimate the extent of penetration into the stable layer above a stellar-type convection zone by varying the rotation rate (Ω), the inclination of the rotation vector (θ) and the relative stability (S) of the upper stable layer. The computational domain is a rectangular box in an f-plane configuration and is divided into two regions of unstable and stable stratification with the stable layer placed above the convectively unstable layer. Several models have been computed and the penetration distance into the stable layer above the convection zone is estimated by determining the position where time averaged kinetic energy flux has the first zero in the upper stable layer. The vertical grid spacing in all the model is non-uniform, and is less in the upper region so that the flows are better resolved in the region of interest. We find that the penetration distance increases as the rotation rate increases for the case when the rotation vector is aligned with the vertical axis. However, with the increase in the stability of the upper stable layer, the upward penetration distance decreases. Since we are not able to afford computations with finer resolution for all the models, we compute a number of models to see the effect of increased resolution on the upward penetration. In addition, we estimate the upper limit on the upward convective penetration from stellar convective cores.

Keywords convection – stars · interior – Sun · interior – rotation.

PACS First · Second · More

1 Introduction

Simulations of penetrative convection above a stellar-type convection zone have been performed in two-dimensions by Hurlburt et al. (1986), and in three-dimensions by Singh et al. (1994, 2001) and

Partha S. Pal
Department of Physics & Astrophysics, University of Delhi, Delhi - 110 007, India

Harinder P. Singh
Department of Physics & Astrophysics, University of Delhi, Delhi - 110 007, India
E-mail: hpsingh@physics.du.ac.in

Kwing L. Chan
Department of Mathematics, Hong Kong University of Science & Technology, Hong Kong, China

M. P. Srivastava
Department of Physics & Astrophysics, University of Delhi, Delhi - 110 007, India

Robinson et al. (2004). In the studies by Hurlburt et al. and Singh et al., several models were computed to study the overshoot of convective motions from unstable into the upper stable layer in a non-rotating configuration. It was found that the motions from the convective region penetrate a significant fraction of pressure scale height into the stable layer above. Singh et al. (1994) also found that the penetration distance above the convection zone (Δ_u) scales as $\Delta_u \sim (F_b/\rho_{ctop})^{1/3}$, where F_b is the input flux and ρ_{ctop} is the density at the top of the convection zone. Robinson et al. (2004) performed three-dimensional simulations of the upper radiation-convection transition layer with more realistic modeling for three subgiant stars. For the present Sun they found the overshoot to be $0.5H_p$, for the 11.3-Gyr subgiant it was $0.75H_p$, while for a 11.6-Gyr subgiant it was approximately $1H_p$, H_p being the local pressure scale height.

Simulations of the effects of rotation on convective penetration or overshooting have been studied by Brummel et al. (2002), Ziegler & Rüdiger (2003), Browning et al. (2004), Käpylä et al. (2004), and Pal et al. (2007). Brummel et al. (2002) and Pal et al. (2007) examined the behaviour of penetrative convection below a convection zone under the influence of rotation by means of three-dimensional simulations. They found that with an increase in rotational velocity, the downward penetration decreased. A similar behaviour was observed when the stability of the lower stable layer was increased in a rotating configuration. Furthermore, the relative stability parameter S showed an $S^{-1/4}$ dependence on the penetration distance implying the existence of a thermal adjustment region in the lower stable layer rather than a nearly adiabatic penetration zone. Ziegler & Rüdiger (2003) and Käpylä et al. (2004), using their 3D MHD codes also found that, as a general feature, the overshooting at the bottom decreases as a function of increasing rotation at a given latitude.

Browning et al. (2004) performed three-dimensional simulations of core convection within A-type stars at a range of rotation rates. They found that as convective motions enter the stable stratification of the radiative envelope, increasing the rotation rate enhances the overshooting.

In this paper, we perform large eddy simulations of turbulent convection in a f -plane configuration to study the effect of rotation on the penetration distance above the convection zone. A total of 17 two-layer (lower unstable – upper stable) models have been set up to examine the effect of rotation rate (Ω) and colatitude (θ) on the penetration distance. In some models, we systematically vary the stability of the upper stable layer to study its effect on the penetration distance. In one model, we increase the horizontal resolution to see if the penetration distance is altered.

In the next section, we give the essential ingredients of the simulations and the parameters of the computed models. In Section 3, we provide the results and their discussion. Important conclusions of the study are listed in Section 4.

2 Parameters of Computed Models

The general behaviour of convective transport in a stellar-type setting has been studied using Large Eddy Simulation (LES) approach by several groups (Chan & Sofia 1986, Hossain & Mullan 1991, 1993, Muthsam et al. 1995, Singh & Chan 1993, Singh et al. 1994, 1995, 1996, 1998a,b, 2001 Saikia et al. 2000, Chan 2001, Pal et al. 2007). LES, being less demanding on speed and memory as it can have a coarser grid, allows large scale flows to be modeled explicitly while the smaller scales are modeled by some sort of sub-grid scale formulation (Smagorinsky 1963).

Pal et al. (2007) numerically solved the Naviér-Stokes equations and incorporated the rotational effects by considering an f -plane configuration. A plane parallel layer of perfect gas was considered in a rectangular box which can be viewed as a small portion of a spherical shell. We use a configuration that is similar to that of Pal et al. (2007) except that the computational domain has two layers (lower unstable – upper stable) rather than their three layer sandwich (stable-unstable-stable) configuration. The choice is justified as we are interested in studying the behaviour of penetrative convection above a convection zone rather than below as was the aim of Pal et al. (2007). The spherical shell rotates around the polar axis from west to east and the angular velocity vector Ω points toward the north pole. We use a right handed cartesian coordinate system in which X and Y denote the horizontal direction and Z denotes the upward vertical direction. The gravity vector is denoted by \mathbf{g} and is along the negative Z direction. The angle between Ω and the Z axis is denoted by θ and the rotation vector Ω lies in the XZ plane. The tilted rotation vector is kept constant implying a uniform angular velocity of the sphere.

Table 1 Physical Parameters for Models R1 to R17

Models	Grid	F_b	Polytropic Indices			Layer Thickness(PSH)			
			Top	Bottom	P_b	T_b	ρ_b	Top	Bottom
R1-R13	$35 \times 35 \times 96$	0.125	2.0	1.5	4655	19.5	238	6.04	2.40
R14	$35 \times 35 \times 96$	0.125	3.0	1.5	19767	17.8	1106	7.12	2.77
R15	$35 \times 35 \times 96$	0.125	4.0	1.5	65092	16.8	3862	8.01	3.07
R16	$35 \times 35 \times 96$	0.125	5.0	1.5	178290	16.1	11024	8.76	3.33
R17	$46 \times 46 \times 96$	0.125	2.0	1.5	4655	19.5	238	6.04	2.40

The rectangular computational domain has an aspect ratio of 1.5 and a mesh of $35 \times 35 \times 96$ points. The top and bottom boundaries are kept impenetrable and stress-free while the side boundaries are made periodic. The domain is divided into two layers with the convectively unstable layer positioned below the convectively stable one. A constant flux \mathbf{F}_b is fed from the bottom and all the thermodynamic variables are expressed in units which set the total depth and initial density, pressure and temperature at the top to unity.

We use the Large Eddy Simulations (LES) approach to solve the Navier-Stokes equation for an ideal gas having the ratio of specific heats (γ) as 5/3. The equations of the problem are given in Pal et al. (2007). We use the Smagorinsky coefficient of viscosity to represent the sub-grid-scale eddy viscosity in the form:

$$\mu = \rho(c_\mu \Delta)^2 (2\sigma : \sigma)^{1/2}, \quad (1)$$

where c_μ is the Deardorff coefficient (Deardorff 1971), σ is the strain rate tensor and the colon sign inside the bracket denotes tensor contraction and $\Delta^2 = (\Delta_x \Delta_y)^{1/2} \Delta_z$. The SGS turbulent diffusivity is computed from this viscosity by assuming a constant Prandtl number $Pr = 1/3$

The governing fluid equations are solved using an implicit scheme (Chan & Wolf 1982) and the time step is characterized by the CFL number

$$N_{CFL} = C_s \Delta t / \Delta_{min}, \quad (2)$$

where Δ_{min} is the minimum grid size in any direction and $C_s = \gamma^{1/2}$ is the dimensionless sound speed at the top. The boundary conditions imposed are :

$$\mathbf{F}_b = \text{constant} = 0.125 \quad (\text{at the bottom}),$$

$$T = T_t = \text{constant} \quad (\text{at the top}),$$

$$v_z = 0; \quad \frac{\partial v_x}{\partial z} = \frac{\partial v_y}{\partial z} = 0.$$

We have computed 17 models and the physical parameters for the models are listed in Table 1. The numerical parameters of the simulations are given in Table 2. Columns (6) - (9) in Table 3 list the values of Coriolis number (Co), Rossby number (Ro), effective Reynolds number (Re), and Taylor number (Ta) for the simulated cases. Following Chan (2001), they are defined as

$$Co = \Omega d / \langle v'' \rangle,$$

$$Ro = 1/Co,$$

$$Re = \langle v'' \rangle d / \langle \bar{\mu} / \bar{\rho} \rangle,$$

$$Ta = (2\Omega d^2 / \langle \bar{\mu} / \bar{\rho} \rangle)^2,$$

with $v'' \equiv (v_x''^2 + v_y''^2 + v_z''^2)^{1/2}$ where v_x'' denotes the root mean square (rms) fluctuation of v_x etc. The extent of domain is denoted by d .

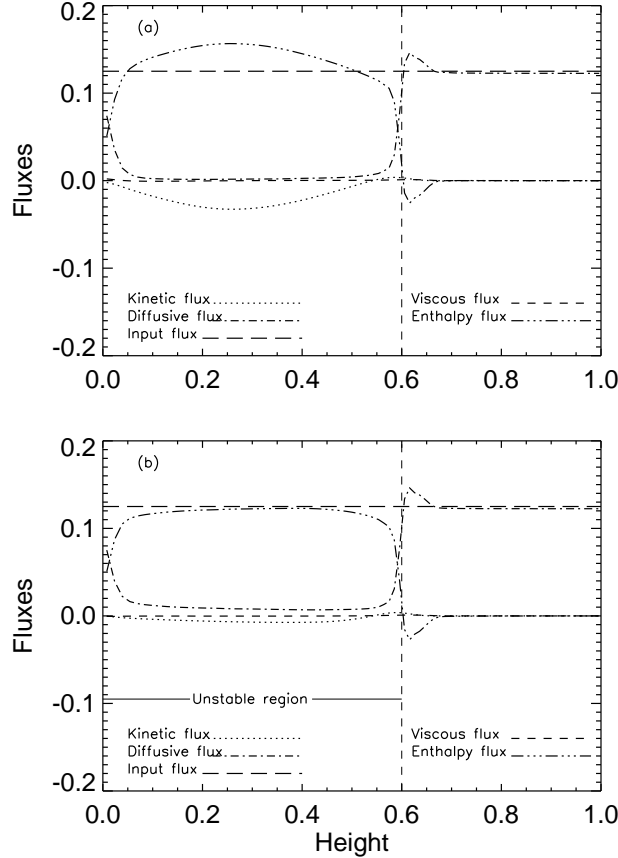


Fig. 1 Profiles of the time- and horizontally-averaged energy fluxes for (a) case R1 ($\Omega = 0$, $\theta = 0^\circ$), (b) case R7 ($\Omega = 0.5$, $\theta = 45^\circ$).

Models R1 to R13 are computed to examine the effect of rate of rotation (Ω) and the angle (θ) between the rotation vector and the vertical axis on the extent of penetration below the convectively stable layer. The polytropic index of the upper stable layer is taken to be 2.0 in all these models (R1-R13). In models R2 to R5, θ is varied from 22.5° to 90° while Ω is fixed at 0.25. In the second set of models R0, R10, R11 and R13, Ω is varied from 0 to 1 in steps of 0.25, respectively, keeping θ fixed at 0° . In models R3, R7, and R12, Ω is 0.25, 0.5 and 1.0, respectively, while θ is fixed at 45° . In the last set of models R14 to R16, polytropic index of the upper stable layer is varied from 3 to 5 while all the other parameters are the same as model R7. Another model R17, having a grid of $46 \times 46 \times 96$ points and all other parameters same as R7 ($\Omega = 0.5$, $\theta = 45^\circ$) is computed to examine the effect of increase in the number of grid points (resolution) in the horizontal plane.

As described, four models, namely, R7, R14, R15 and R16 have been set-up to examine the effect of stability of the upper stable layer on the penetration height of these rotating configurations. Each of these four models have different polytropic indices in the upper stable layer, namely, 2, 3, 4 and 5 for the cases R7, R14, R15 and R16, respectively. For all these four models, the values of Ω and θ are kept constant at 0.5 and 45° respectively. Similar to the relative stability parameter S for the lower stable layer (Hurlburt et al. 1994, Singh et al. 1995, Pal et al. 2007), we can define a relative stability parameter for the upper stable layer for these four cases as:

$$S = \frac{m_i - m_a}{m_2 - m_a} ; m_i = 2, 3, 4, 5, \quad (3)$$

where m_i denote the polytropic indices of the upper stable layer for various cases, m_2 is the polytropic index of the upper stable layer for our case R7 and $m_a = 1/(\gamma - 1)$ is the adiabatic index. Here, we have taken $\gamma = c_p/c_v$ as $5/3$. Thus, for our reference case R7 the relative stability parameter S is equal to unity and for cases R14, R15 and R16 it comes out to be 3, 5 and 7, respectively.

Table 2 Numerical Parameters for the 17 models

Models	g	C_μ	Δt	t	N_{CFL}	Δ_{\min}
R1-R15,R17	50	0.2	0.00054795	1698	0.1	0.007074
R16	50	0.2	0.00027397	1698	0.05	0.007074

Table 3 Dynamical Parameters of the Computed Models

Model	Ω	θ/π	θ	$\langle v'' \rangle$	Co	Ro	Re	Ta	Δ_u	Δ_p (PSH)
R1	0	0	0°	0.074	0.000	∞	1088.883	0.00E+0	0.055	0.384
R2	0.25	1/8	22.5°	0.059	4.231	0.236	894.394	5.728E+7	0.057	0.399
R3	0.25	1/4	45°	0.064	3.914	0.255	947.021	5.502E+7	0.057	0.399
R4	0.25	3/8	67.5°	0.070	3.579	0.279	1022.810	5.360E+7	0.051	0.354
R5	0.25	1/2	90°	0.066	3.776	0.265	957.403	5.227E+7	0.031	0.210
R6	0.50	1/4	22.5°	0.056	8.980	0.111	840.540	2.279E+8	0.060	0.422
R7	0.50	1/4	45°	0.059	8.432	0.119	879.430	2.200E+8	0.055	0.385
R8	0.50	1/4	67.5°	0.067	7.411	0.135	975.684	2.091E+8	0.052	0.362
R9	0.50	1/2	90°	0.064	7.795	0.128	875.589	1.864E+8	0.022	0.147
R10	0.25	0	0°	0.058	4.278	0.234	889.006	5.787E+7	0.058	0.407
R11	0.50	0	0°	0.054	9.283	0.108	822.673	2.331E+8	0.063	0.445
R12	1.0	1/4	45°	0.069	14.474	0.069	1011.623	8.576E+8	0.052	0.363
R13	1.0	0	0°	0.050	20.004	0.050	768.311	9.448E+8	0.063	0.446
R14	0.50	1/4	45°	0.036	13.714	0.073	876.052	5.774E+8	0.013	0.111
R15	0.50	1/4	45°	0.026	19.013	0.053	895.473	1.160E+9	0.006	0.061
R16	0.50	1/4	45°	0.019	25.469	0.039	799.152	1.659E+8	0.005	0.058
R17	0.50	1/4	45°	0.062	7.971	0.126	1107.676	3.118E+8	0.049	0.340

3 Results and Discussion

All 17 models computed in this study have a two layer configuration in which the stable region is placed above the convectively unstable region. Model R1 is non-rotating while models R2 to R17 are all rotating, differentiated by a set of values of rate of rotation (Ω), the angle between the Z -axis and the rotation vector (θ) and the polytropic index (or stability) of the upper stable layer. Tables 1 and 2 list the physical parameters of all the models.

The interface of the unstable-stable layer is located at a height of 0.6 from the bottom. This implies that the thickness of the lower stable layer is 0.6 or 60% of the total domain of computation while the upper stable layer has a thickness of 0.4 corresponding to 40% of the total domain. The total domain of computation contains about 8.44 pressure scale heights (PSH) for models R1-R13 and R17 with the upper stable layer containing 6.04 PSH while the lower convective layer contains 2.40 PSH. For models R14, R15 and R16 the total domain has around 9.89, 11.08 and 12.09 PSH, respectively with the upper stable layer containing around 7.12, 8.01 and 8.76 PSH, respectively.

It may be noticed that although the upper stable layer occupies only 40% of the domain, it contains more than 70% of the PSH. This is because the length of the PSH decreases as we go from bottom to the top. The density contrast ($\rho_{\text{bottom}}/\rho_{\text{top}}$) of models R1-R13 is 238.0 while the temperature contrast ($T_{\text{bottom}}/T_{\text{top}}$) is 19.5 (cf. Table 1). For model R16 the density contrast is the maximum (11024).

After the fluid has thermally relaxed, it is further evolved for another 1,00,000 time steps and the time and horizontal averages are taken for quantities of interest. Figure 1 shows the distribution of various energy fluxes with height for a number of models. The calculation of the extent of the penetration into the upper stable layer has been based on time- and horizontally averaged kinetic flux (F_k). Such a choice is obvious as the kinetic flux is directly related with the motions and the profile is also convenient for estimation of the extent of penetration (Hurlburt et al. 1986, Hurlburt et al. 1994, Singh et al. 1994,1995, Saikia et al. 2000, Pal et al. 2007). We illustrate this point by plotting the distribution of kinetic energy flux for several sets of models in Fig. 2. The kinetic energy flux is negative in most of the convectively unstable region. Near the interface in the unstable region it increases and becomes positive and then falls to zero in the upper stable region. Ideally, the extent of penetration should correspond to the first zero of the kinetic energy flux in the stable layer above the unstable-stable interface. However, we define the penetration height (Δ_u) to be the distance from the interface of the unstable-upper stable layer to where F_k has fallen to a value of 0.0001 in the upper

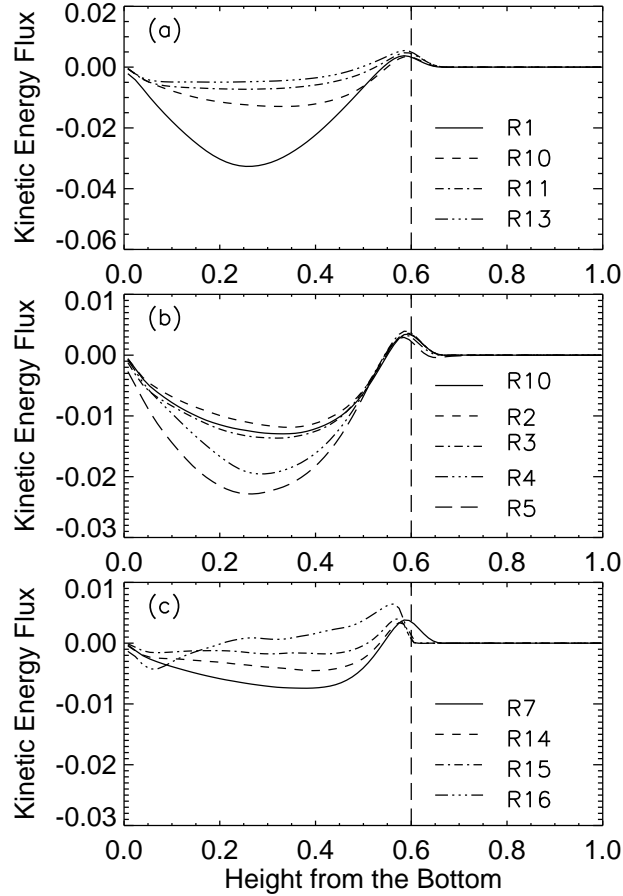


Fig. 2 Distribution of time- and horizontally averaged kinetic energy fluxes with height for models (a) R1, R10, R11 and R13. The corresponding values of angular rotational velocity (Ω) are 0, 0.25, 0.50 and 1.0, respectively. For these four cases the angle (θ) between the rotation vector and the vertical axis is 0° , (b) R10, R2, R3, R4 and R5. All these models have Ω fixed at 0.25 while θ changes from 0° to 90° in steps of 22.5° , (c) R7, R14, R15 and R16. The polytropic indices in the upper stable layer for these four models are, respectively, 2, 3, 4 and 5. The corresponding relative stability parameters are 1, 3, 5 and 7, respectively. All the four models have $\Omega = 0.5$ and $\theta = 45^\circ$.

stable layer. The extent of penetration distance (Δ_u) and penetration distance in PSH (Δ_p) for all the 17 models are given in Table 3.

In Fig. 3(a), we show the horizontally averaged kinetic energy flux as a function of depth and time for model R1. We have plotted 500 profiles of F_k which corresponds to every 200th time step. In Fig. 3(b), we show a time series of penetration distance Δ_u calculated by using the criterion outlined above. The mean penetration is indicated by the horizontal dashed line.

We now describe the effect of varying various parameters, e.g., Ω , θ , S , and the horizontal resolution on the penetration distance above the convectively unstable region.

3.1 Dependence of penetration height on Ω

Two sets of models R1, R10, R11 and R13 and R3, R7 and R12 have been computed to examine the effect of rate of rotation on the penetration distance. In models R1, R10, R11 and R13, the rotation rate (Ω) is systematically increased from 0 to 1.0 in steps of 0.25 (cf. Table 3). In all these four models, the rotation vector (θ) is kept at 0° , implying that the rotation vector coincides with the Z -axis or the vertical direction. Figure 4(a) shows the dependence of penetration distance on Ω for these four models. In model R1, which is a non-rotating case ($\Omega = 0$), the penetration distance $\Delta_u = 0.055$ or 0.384 PSH. As the rotation rate increases to 0.25 in model R10, the distance Δ_u increases to 0.058

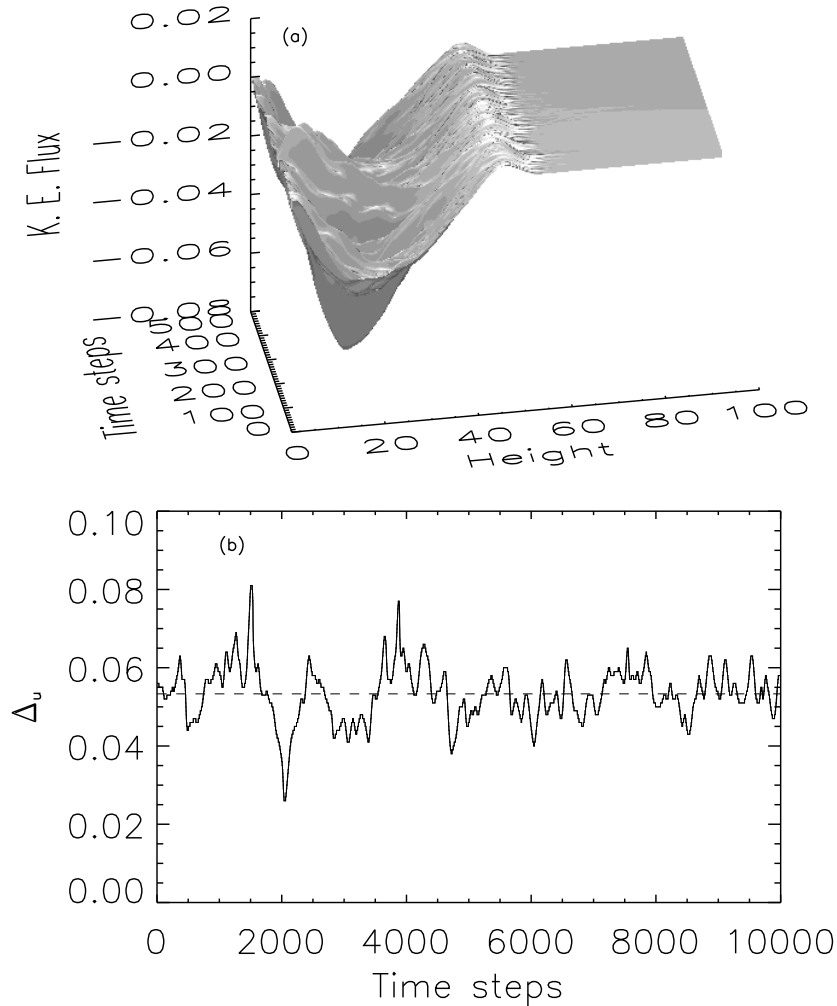


Fig. 3 (a) Horizontally averaged kinetic energy flux as a function of time. Total of 1,00,000 profiles were collected out of which 500 (every 200th) are plotted for case R1. The height is denoted in the grid points starting from one at the bottom (b) Penetration height (Δ_u) with time for model R1 for 1,00,000 time steps (computed at every 10th time step).

which corresponds to 0.407 PSH. For models R11 and R13 having $\Omega = 0.5$ and 1.0 respectively, the penetration distance increases further to 0.445 PSH and 0.446 PSH respectively.

In the second set of models R3, R7 and R12, while the rotation rates are, respectively, 0.25, 0.5 and 1.0, θ is changed to 45° . We find that unlike in the first set of models (with $\theta = 0^\circ$), the penetration distance decreases with increase in the rotation rate. For example, the upward penetration decreases from 0.399 PSH (Model R7, $\Omega = 0.25$) to 0.363 PSH (Model R12, $\Omega = 1.0$). The buoyancy-breaking is accentuated as rotation rate is increased when θ is 45° .

The penetrative behaviour is markedly different from the case of downward penetration (Pal et al. 2007), in which the penetration distance (Δ_d) decreased with increase in the rotation rate, for any fixed value of colatitude θ .

For the two sets of models with $\theta = 0^\circ$ and $\theta = 45^\circ$, we examine the behaviour of penetration height with Rossby number. Figure 5(a) shows the variation of penetration height in PSH (Δ_p) with Rossby number (Ro) for three cases R10, R11 and R13 having $\theta = 0^\circ$ and $\Omega = 0.25, 0.50$ and 1.0, respectively. A smaller Rossby number implies a larger rotation rate and the penetration distance increases with decrease in the Rossby number from 0.407 PSH for model R10 to 0.446 PSH for model R13. For this set of models with $\theta = 0^\circ$, we see a relationship $\Delta_p \sim 0.38 Ro^{-0.059}$.

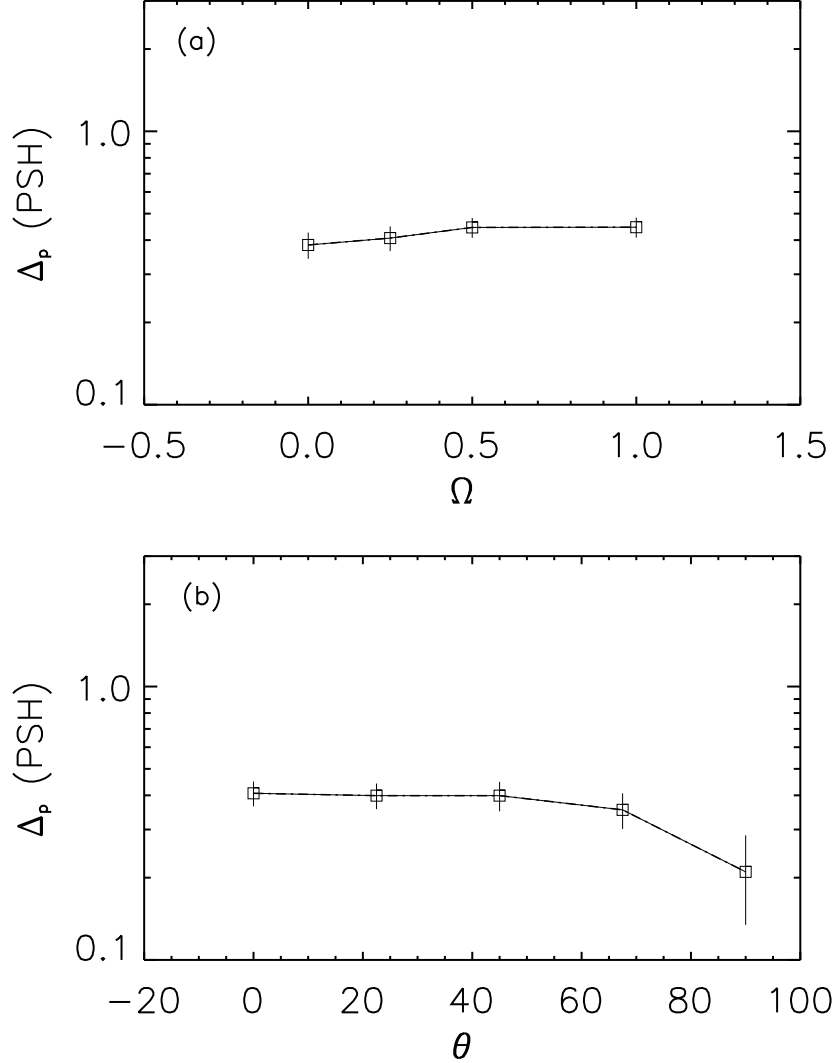


Fig. 4 Dependence of penetration height in PSH (Δ_p) with (a) Ω varying from 0, 0.25, 0.50 and 1.0 for the models R1, R10, R11 and R13, (b) colatitude (θ) varying from 0° to 90° in steps of 22.5° for models R10, R2, R3, R4 and R5 having $\Omega = 0.25$. In this as well as in all the subsequent figures, error bars denote the standard deviation in Δ_p computed for 1,00,000 time steps after the fluid has thermally relaxed.

Fig. 5(b) shows the variation of Δ_p with Ro for the second set of models R3, R7 and R12 having $\theta = 45^\circ$ and $\Omega = 0.25, 0.50$ and 1.0 , respectively. For this set, the penetration distance decreases with the decrease in Rossby number. Model R3 with $Ro = 0.255$ has $\Delta_p = 0.399$ PSH, while R12 with $Ro = 0.069$ has $\Delta_p = 0.363$ PSH. This set of models shows a scaling relation of $\Delta_p \sim 0.44 Ro^{0.072}$.

3.2 Dependence of penetration height on colatitude θ

A set of five models R10, R2, R3, R4 and R5 has been examined to study the effect of co-latitude (θ) on the penetration distance. All the models have $\Omega = 0.25$ while θ is changed from 0° (Model R10) to 90° (Model R5) in steps of 22.5° . Figure 4(b) shows the plot of Δ_p against θ for these five models. At $\theta = 0^\circ$, the penetration distance is maximum 0.407 PSH. It decreases slightly for successive values of θ , and for $\theta = 90^\circ$ (case R5) has the minimum value of 0.210 PSH.

Singh et al. (1994) computed many non-rotating cases having different input fluxes and found a scaling relationship between the upward penetration and the input flux (F_b) of the form $\Delta_p \sim$

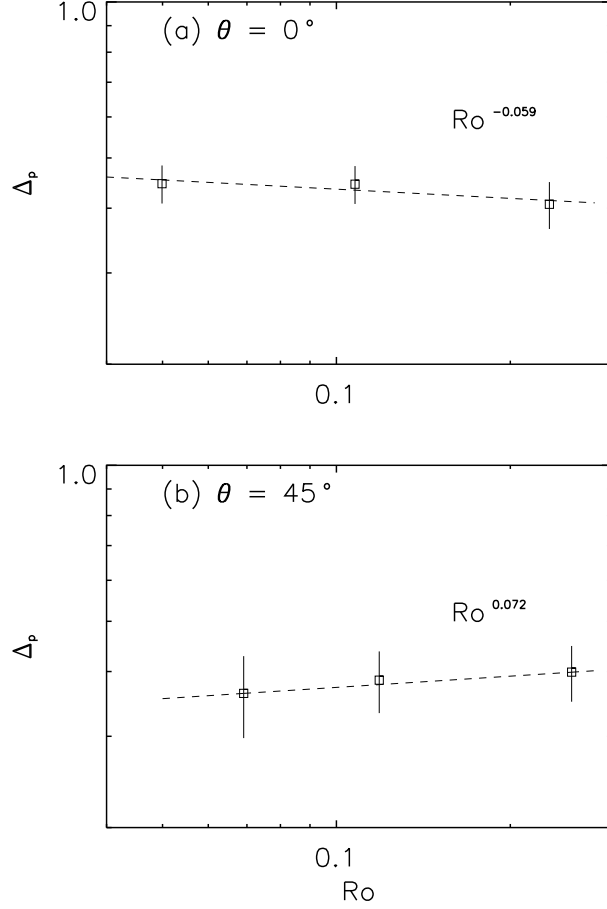


Fig. 5 Variation of penetration height with Rossby number for (a) three models R10, R11 and R13 having $\Omega = 0.25, 0.50$ and 1.0 , respectively, and $\theta = 0^\circ$, and (b) three models R3, R7 and R12 having $\Omega = 0.25, 0.50$ and 1.0 , respectively, and $\theta = 45^\circ$. The dashed lines represent scaling laws: (a) $Ro^{-0.059}$ and (b) $Ro^{0.072}$.

$(F_b/\rho_{ctop})^{1/3}$, where ρ_{ctop} is the density at the top of the convection zone. We attempt to find a similar relationship which includes the effects of rotation.

In Fig. 6(a), we have plotted $(F_b/\rho_{ctop})^{1/3}/\Delta_p$ for $\Omega = 0.25, 0.5$, and 1.0 corresponding to models R10, R11, and R13, respectively. We find a scaling relationship $\Delta_p \sim (F_b/\rho_{ctop})^{1/3}/0.283(\Omega)^{-0.065}$ for the three cases having $\theta = 0^\circ$. For cases R3, R7, R12 having $\theta = 45^\circ$ (Fig. 6(b)), we have a relationship of the form $\Delta_p \sim (F_b/\rho_{ctop})^{1/3}/0.35(\Omega)^{0.068}$.

For a set of models with a particular value of θ , we have

$$\Delta_p = c_1 Ro^{x_1} \quad \text{and} \quad \Delta_p = \frac{(F_b/\rho_{ctop})^{1/3}}{c_2 \Omega^{x_2}}, \quad (4)$$

where c_1 and c_2 are constants and x_1 and x_2 are the scaling powers for Ro and $1/\Omega$.

One can use relations (4) to compute back the power laws of Fig. 6 by writing

$$\Omega^{x_2} = \frac{(F_b/\rho_{ctop})^{1/3}}{c_1 c_2 Ro^{x_1}}, \quad (5)$$

$$x_2 = \frac{\ln \frac{(F_b/\rho_{ctop})^{1/3}}{c_1 c_2 Ro^{x_1}}}{\ln \Omega}. \quad (6)$$

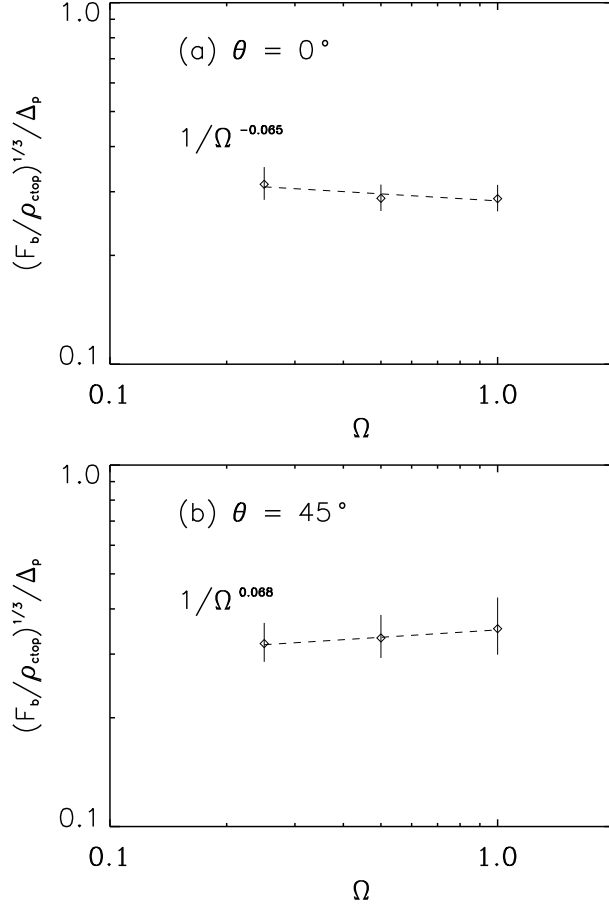


Fig. 6 Plot of $(F_b/\rho_{ctop})^{1/3}/\Delta_p$ for different Ω for (a) cases R10, R11 and R13 having $\theta = 0^\circ$ and (b) cases R3, R7, R12 having $\theta = 45^\circ$. The dashed line shows the scaling relationship (a) $1/\Omega^{-0.065}$ and (b) $1/\Omega^{0.068}$ for the two sets of models.

Substituting the value of Ro , c_1 , c_2 , x_1 , and Ω in Eqn.(6), we find that for cases with $\theta = 0^\circ$, x_2 to be -0.063 and for cases with $\theta = 45^\circ$ it is 0.062 which are close to the values -0.065 and 0.068 , respectively, as shown in Fig. 6.

3.3 Dependence of penetration height on relative stability parameter S

We have constructed four models with different stability parameter (S) defined in Eqn. (3) by varying the polytropic index of the upper stable layer. We have $S = 1, 3, 5$ and 7 for cases R7, R14, R15 and R16, respectively. In Fig. 2(c), we have plotted the distribution of the kinetic energy flux with height for these four models. The values of the angular velocity (Ω) and angle between the rotation vector and vertical axis (θ) are fixed at 0.5 and 45° , respectively, for these models. The corresponding penetration heights Δ_u and Δ_p (in PSH) are given in the last two columns of Table 3. Figure 2(c) clearly shows the differences in the kinetic flux profile with S especially in the region near the stable-unstable layer interface. We find a decrease in penetration distance from 0.385 PSH in model R7 ($S = 1$) to 0.058 PSH in model R16 ($S = 7$). Figure 7 shows the instantaneous vertical velocities at the horizontal interface of the unstable-stable interface for models R7 and R16. The vertical velocities for model R16 with stiffer stable layer ($S=7$) are much lower compared to that of model R7 ($S=1$).

Fig. 8 shows the variation of penetration distance with stability factor S for models R7, R14, R15, & R16. These models show a scaling relationship $\Delta_p \sim S^{-1}$. This means that the convection is efficient enough to establish a nearly adiabatic stratification in the upper stable layer and the penetration is nearly adiabatic (Hurlburt et al. 1994, Zahn 2002). Brummel et al. (2002) and Pal et al. (2007) found a

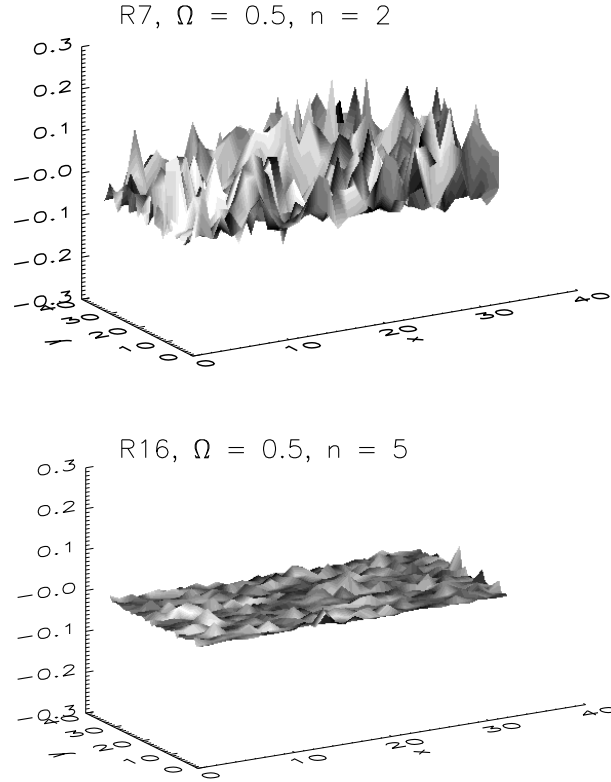


Fig. 7 Instantaneous vertical velocity at a horizontal surface at unstable-upper stable layer boundary located at a height of 0.6 from the bottom for two cases R7 ($\Omega = 0.5$, $\theta = 45^\circ$) and R16 ($\Omega = 0.5$, $\theta = 45^\circ$). Polytropic indices of the upper stable layer are 2 (Model R7) and 5 (Model R16).

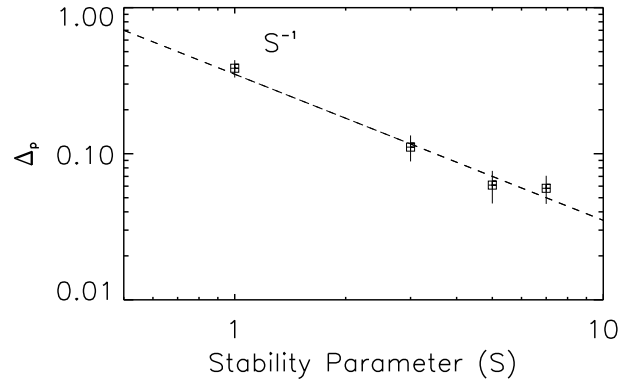


Fig. 8 Variation of penetration distance Δ_p with stability parameter S for models R7, R14, R15 and R16. Here, $\Omega = 0.5$ and $\theta = 45^\circ$. The dashed line represents scaling law, S^{-1} .

scaling relationship of $\Delta_p \sim S^{-1/4}$ for downward penetration for rotating convection zones associated with a thermal adjustment region at the bottom.

3.4 Dependence of penetration height on resolution

Table 4 lists additional models computed to see the effect of resolution on the upward penetration. Model R1A is same as model R1 except that it has a total of 524,288 ($64 \times 64 \times 128$) grid points instead of 117,600 ($35 \times 35 \times 96$) grid points, having better horizontal as well as vertical resolution.

Table 4 Parameters of models computed to examine the effect of resolution on the upward penetration

Models	Grid	Ω	θ/π	θ	t	Δ_p (PSH)
R1A	$64 \times 64 \times 128$	0	0	0°	1056	0.303
R7A	$64 \times 64 \times 128$	0.50	1/4	45°	907	0.333
R7B	$96 \times 96 \times 96$	0.50	1/4	45°	550	0.268

Table 5 Penetration as a percentage of the size of the Convection Zone

Model	R1	R2	R3	R4	R5	R6	R7	R8	R9	R10	R11	R12	R13
% Δ_p	16.0	16.6	16.6	14.8	8.8	17.6	16.0	15.0	6.0	17.0	18.5	15.1	18.6
Model	R14	R15	R16	R17									
% Δ_p	4.0	2.0	1.7	14.2									

Penetration height for non-rotating model R1 is 0.384 PSH (cf. Table 3), while for the non-rotating model R1A with increased resolution, it is 0.303 PSH.

Two rotating models R7 and R7A examine the effect of change in both horizontal and vertical resolution on the penetration distance. We notice a decrease in penetration depth from 0.385 PSH in model R7 ($35 \times 35 \times 96$) to 0.333 PSH in model R7A ($64 \times 64 \times 128$). It may be noticed that while models R1 and R7 had almost same penetration distance, the decrease in Δ_p with increased resolution is smaller for model R7A which has a higher rotation rate compared to model R1A which is non-rotating. It seems that the effect of increase in resolution on penetration is different for models with different rotation rates.

Three models R7, R17, and R7B examine the effect of horizontal resolution on the penetration distance above the convection zone. While all the models have 96 grid points in the vertical, they differ in their horizontal resolution. Model R7 has 35×35 grid points in the horizontal direction, model R17 has 46×46 and model R7B has 96×96 grid points. The penetration distance decreases with the increase in horizontal resolution from 0.385 PSH (Model R7) to 0.340 PSH (Model R17) to 0.268 PSH (Model R7B).

4 Conclusions

We have computed 17 models and presented the results of our three-dimensional numerical simulations of turbulent compressible convection penetrating into a radiative envelope under the influence of rotation. We find that the penetration distances for these models lie in the range $0.058 \text{ PSH} \leq \Delta_p \leq 0.446 \text{ PSH}$.

Recently, Woo & Demarque (2001) put an empirical constraint on the convective core overshoot for intermediate-to-low mass stars by using Roxburgh's integral constraint. They found that the proper limit of core overshoot for these stars would be 15% of the core radius. In Table 5, we have shown this calculation for our 17 models. We have computed the penetration distance in PSH as a percentage of the total size of the convection zone. The size of the convection zone is taken from the last column of Table 1 while the penetration height (Δ_p) has been taken from the last column of Table 3. As can be seen from Table 5, We find an upper limit on the penetration into the upper radiative layer to be around 18.5%.

For rotation about a vertical axis ($\theta = 0^\circ$), the penetration into the upper stable region increases as the angular rotational velocity (Ω) increases or the Rossby number (Ro) decreases. However, this trend is reversed for rotation around an inclined axis. When the angle ($\theta = 45^\circ$), the penetration distance into the radiative envelope decreases with increasing Ω owing to horizontal mixing. To see the effect of change of angle of inclination on penetration, angle θ is systematically varied from 0° to 90° in steps of 22.5° for five models with a fixed angular velocity $\Omega = 0.25$. We again find that the penetration distance decreases as the colatitude θ is increased. We do not see this behaviour changing even when the resolution is increased.

We also find that the penetration distance above the convection zone obeys a scaling relation of the form $\Delta_p \sim S^{-1}$ appropriate for nearly adiabatic penetration even in the presence of rotation. The present simulations need to be extended to include more realistic input physics and a higher resolution to enable us to get a better insight into the dynamics of rotating convection near the convective-

radiative interface. Since the motivation of the study was to look into the effect of varying rotation rates on the penetration distance, we needed to compute several models. Due to the restrictions in speed and memory, we were unable to increase the resolution of all the models. We hope to achieve this in future studies.

Acknowledgements PSP is grateful to University Grants Commission, India for a Senior Research Fellowship. HPS was supported by grants from Indian Space Research Organization and Deutscher Akademischer Austauschdienst (DAAD), Germany. KLC was partly supported by grants from Hong Kong Research Grant Council. Authors acknowledge the use of High Performance Computing facilities at IUCAA, Pune, India.

References

1. Browning, M. K., Brun, A. S., Toomre J.: *ApJ*, **601**, 512 (2004)
2. Brummell, N. H., Clune, T. L., Toomre J.: *ApJ*, **493**, 955 (2002)
3. Chan K. L.: *ApJ*, **548**, 1102 (2001)
4. Chan K. L., Sofia S.: *ApJ*, **307**, 222 (1986)
5. Chan K. L., Sofia S.: *ApJ*, **336**, 1022 (1989)
6. Chan K. L., Wolff C. L.: *J. Comput. Phys.*, **47**, 109 (1982)
7. Deardorff J. W.: *J. Comput. Phys.*, **47**, 109 (1971)
8. Hossain M., Mullan D. J.: *ApJ*, **380**, 631 (1991)
9. Hossain M., Mullan D. J.: *ApJ*, **416**, 733 (1993)
10. Hurlburt N. E., Toomre J. M., Massaguer J. M.: *ApJ*, **311**, 563 (1986)
11. Hurlburt N. E., Toomre J. M., Massaguer J. M., Zahn J. -P.: *ApJ*, **421**, 245 (1994)
12. Käpylä P. J., Korpi M. J., Stix M. J., Tominen I.: *A&A*, **438**, 403 (2005)
13. Muthsam H. J., Göb W., Kupka F., Leibich W., Zöchling J.: *A&A*, **293**, 127 (1995)
14. Pal, P. S., Singh, H. P., Chan, K. L., Srivastava, M. P.: *AP&SS*, **307**, 399 (2007)
15. Robinson, F. J., Demarque, P., Li, L.H. et al.: *MNRAS*, **347**, 1208 (2004)
16. Saikia E., Singh H. P., Chan K. L., Roxburgh I. W., Srivastava M. P.: *ApJ*, **529**, 402 (2000)
17. Singh H. P., Chan K. L.: *A&A*, **279**, 107 (1993)
18. Singh H. P., Roxburgh I. W., Chan K. L.: *A&A*, **281**, L73 (1994)
19. Singh H. P., Roxburgh I. W., Chan K. L.: *A&A*, **295**, 703 (1995)
20. Singh H. P., Roxburgh I. W., Chan K. L.: *Bull. Astron. Soc. India*, **24**, 281 (1996)
21. Singh H. P., Roxburgh I. W., Chan K. L.: in *ASP Conf. Ser. 138*, Proc. 1997 Pacific Rim Conf. on Stellar Astrophysics, (eds.) K. L. Chan, K. S. Cheng, H. P. Singh (San Francisco: ASP), 313 (1998a)
22. Singh H. P., Roxburgh I. W., Chan K. L.: *A&A*, **340**, 178 (1998b)
23. Singh, H. P., Saikia, E., Roxburgh, I. W., Chan, K. L., Srivastava, M. P.: *ASP Conf. Ser.*, **223**, 874 (2001)
24. Smagorinsky J. S.: *Mon. Weather Rev.*, **91**, 99 (1963)
25. Woo, J. H., Demarque, P.: *ApJ*, **122**, 1602 (2001)
26. Zahn, J. -P.: *ASP Conf. Ser.*, **259**, 58 (2002)
27. Ziegler, U., Rüdiger, G.: *A&A*, **401**, 433 (2003)